Nanoscale

RSC Publishing

PAPER

View Article Online
View Journal | View Issue

Cite this: *Nanoscale*, 2013, **5**, 6874

A simple synthesis method for nano-metal catalyst supported on mesoporous carbon: the solution plasma process†

Jun Kang,*[a] Oi Lun Li[b] and Nagahiro Saito[abc]

High-electrocatalytic-activity noble nanoparticles (NPs) supported on carbon nanoballs (CNBs) were synthesized using an innovative plasma-in-liquid method, which is known as solution plasma processing (SPP). This technique uses a one-step method for the synthesis of NPs on carbon materials. CNBs are formed using benzene as a carbon precursor while gold (Au) or platinum (Pt) nanoparticles are generated instantaneously *via* sputtering from metal electrodes. The synthesized NP/CNBs were annealed at 850 °C in order to increase the conductivity of the material. The results of structural characterizations reveal that the Au and Pt NPs are smaller than 10 nm and have a uniform size distribution, and these NPs are successfully loaded onto highly mesoporous CNBs that have an average pore diameter between 13 and 16 nm. In the results from cyclic voltammetry measurements, the Au/CNBs and Pt/CNBs show clear peaks corresponding to the oxidation and reduction features in the catalytic reactions. Apart from noble nanoparticles, SPP can also be used to synthesize various kinds of NPs including bimetallic NPs loaded on spherical carbon supports by changing the working electrodes. The proposed mechanism for the synthesis is discussed in detail. This method shows potential to be a candidate for the next-generation synthesis of NP/carbon in the future.

Received 11th March 2013
Accepted 15th May 2013

DOI: 10.1039/c3nr01229h

www.rsc.org/nanoscale

Introduction

Noble metal nanoparticles (such as Pt and Au) supported on carbon materials (NP/C) have received great attention because of their unique properties for catalysis, electroanalysis, sensors, fuel cells, and Li-air batteries.[1–8] In particular, they have shown potential for application in direct methanol fuel cells (DMFCs), proton-exchange membrane fuel cells (PEMFCs), and Li-air batteries. These nanoparticles are typically characterized by high activities in oxygen reduction and/or fuel oxidation reactions, because they show a high surface-to-volume ratio and can improve the Fermi levels for redox reactions.[9–11] It is well known that the novel properties and efficiency of nanoparticles are highly dependent not only on their size distribution, but also on the uniformity of their dispersion on the supporting material.[12–15]

The conventional methods for fabricating NP/C materials typically consist of two or three steps: (i) the synthesis of nanoparticles, (ii) the synthesis of carbon materials, and (iii) loading of the nanoparticles on the carbon materials. A variety of preparation routes have been reported for the synthesis of NPs, including reverse micelle processes, salt reduction, microwave dielectric heating reduction, ultrasonic irradiation, radiolysis, solvothermal synthesis, and electrochemical synthesis.[16–24] Among these methods, chemical reduction is the most preferred because of the simplicity of the preparation process and the resulting uniformity in the size distribution. However, this method consists of multiple steps, and requires long treatment times and the use of reducing agents. The additional chemicals introduced in this process lead to high capital costs and add impurities to the synthesized particles.

In the case of carbon supports, although various carbonaceous materials can be applied, particles such as carbon black are typically used as supporting materials. Compared with other carbon materials, carbon black holds advantages in its relative stability in acidic and basic media, its high surface area, its good electronic conductivity, and its comparatively low cost. However, its dense structure limits the diffusion of chemical species into the inner parts of the carbon, leading to poor dispersion and use of the catalyst on its surface. Various methods for the loading of NPs on carbon supports have been investigated. Impregnation or precipitation, colloidal methods, and micro-emulsions are the most commonly used techniques. However, these processes require multiple steps and the use of chemical agents.[25–38]

[a]*Graduate School of Engineering, Nagoya University, Nagoya, 464-8603, Japan. E-mail: kang@rd.numse.nagoya-u.ac.jp; Fax: +81 52 789 2796; Tel: +8152 789 2796*

[b]*Ecotopia Science Research Institute, Nagoya University, Nagoya, 464-8603, Japan. E-mail: helena@rd.numse.nagoya-u.ac.jp; Fax: +81 52 789 3260; Tel: +8152 789 3260*

[c]*Green Mobility Collaborative Research Center, Nagoya University, Nagoya, 464-8603, Japan. E-mail: hiro@rd.numse.nagoya-u.ac.jp; Fax: +81 52 789 5163; Tel: +8152 789 5163*

† Electronic supplementary information (ESI) available. See DOI: 10.1039/c3nr01229h

To overcome these problems, we recently proposed a simple synthesis method for NP/C using solution plasma processing (SPP). The most important merits of SPP, as compared with the above methods, include the short processing time (in the range from a few minutes to several tens of minutes), the fact that the preparation can be performed in room temperature and atmospheric pressure conditions, the simple experimental apparatus, and the fact that no catalysts or agents are required. The process uses a bipolar power supply, pure benzene as a carbon precursor, and a pair of noble metal electrodes. Previous studies showed that the technique could be used to successfully synthesize nanoparticles, including nanocolloidal particles, metal nanoparticles, and carbon-rated materials.[39–44]

The purpose of the present study was to apply the innovative solution plasma process in the field of NP/C synthesis, and to simplify the multiple processes. The structural characterization revealed that the synthesized NPs had a uniform size distribution and an average size of smaller than 10 nm, and were loaded on the highly mesoporous carbon nanoballs (CNBs), which acted as a carbon support during the synthesis process; thus, the synthesis and loading required only one process. The structural properties and the mechanism of the synthetic process were discussed in detail.

Experimental

Solution plasma processing

Experiments were carried out in room temperature and atmospheric pressure conditions. The system consists of two pairs of metal electrodes (gold or platinum, 99.95%, Nilaco, Japan) placed in a glass vessel (100 ml beaker, with a diameter of 5 cm and height of 7 cm) and discharged in benzene (99.5% Kanto chemical, Japan) by a bipolar–DC pulse power supply (Kurita, Japan) (Fig. 1). The reason for using benzene has been described in the ESI (see Fig. S1 and Table S1).† The diameter of the metal electrode was 1 mm. To concentrate energy, electrodes were insulated by ceramic tubes with a protruded length of 1.5 mm from ceramic tube tips. The voltage, pulse frequency, pulse width, and electrode distance were controlled to be 1.6 kV, 25 kHz, 0.5 μs, and 0.5 mm, respectively. The distance between the tips of the electrodes was set to 1 mm. The effects of varying the experimental parameters have also been evaluated (see ESI Fig. S2–S4 and Table S2).†

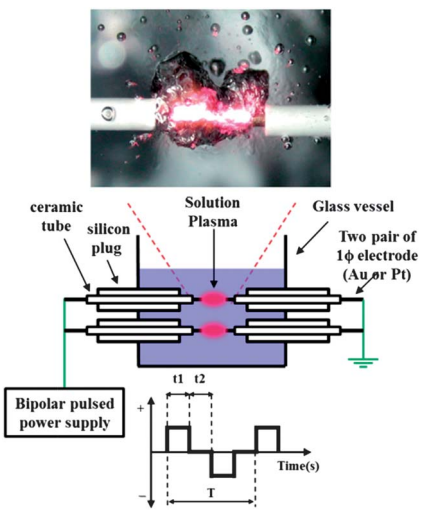

Fig. 1 Schematic of the solution plasma process (SPP).

Drying of sample

To get carbon powder, discharged solution was filtered using a glass microfiber filter (1 μm) and dried in an oven at 70 °C for 1 hour.

Heat treatment

A heat treatment was applied to the CNBs to increase their electrical conductivity for the application of electrochemistry area; this process was performed in a tube furnace with a 20-minute dwell time, under a flowing Ar atmosphere, with a heat treatment temperature (HTTs) of 850 °C (heating rate: 25 °C min^{-1} and cooling rate: 7 °C min^{-1}).

Characterization of NP/CNBs

For the characterization of the CNBs, scanning electron microscopy (SEM) images were obtained using a JSM-6330F (JEOL, Japan) instrument with an accelerating voltage of 5 kV. The shape and microstructure of the NP/CNBs were observed using an annular bright field scanning TEM (ABF-STEM) and a high resolution TEM (HR-TEM), using a JEM-2500SE instrument operated at 200 kV. TEM samples were prepared by dropping the aqueous NP/CNB solution onto a copper grid coated with an ultrathin (about 6 nm) amorphous carbon film without any special treatment. HR-TEM images were recorded close to the Scherzer defocus, and the lattice resolution was 0.14 nm. X-ray diffraction (XRD) patterns were measured using an XRD Rigaku Smartlab (Rigaku, Japan) instrument with Cu Kα radiation (λ = 0.154 nm). The BET surface area, total pore volume, and pore diameter of the NP/CNBs were calculated from N_2 adsorption–desorption isotherms, using the Brunauer–Emmett–Teller (BET) method; these experiments were carried out on Belsorp-mini II (Belsorp, Japan) instruments. Prior to the BET measurements, all of the samples were degassed at 200 °C for 2 hours. Cyclic voltammetry (CV) experiments were performed using a Hokuto Denko Model HZ5000 electrochemical analyzer (Hokuto Denko Inc. Japan). The three-electrode system consisted of a NP/CNB (on a glassy carbon electrode) working electrode, an Ag/AgCl (saturated KCl) reference electrode, and a counter electrode made of platinum wire. The electrochemical working electrodes all had a diameter of 2 mm. Nitrogen gas was bubbled through the electrolyte solution for 30 minutes before the electrodes were characterized; all electrochemical measurements were performed in 100 ml of a 1 M H_2SO_4 solution at room temperature, using scan rates of 20, 50, and 100 mV s^{-1}. In order to understand the plasma chemistry and chemical reaction carried out by radicals in benzene solution, analyses has been carried out by optical emission spectroscopy (OES, Ocean Optics Inst. Co. 200–800 nm) and gas chromatography–mass spectrometry (GC-MS, JMS-Q1050GC, JEOL, Japan).

Results and discussion

Morphology of CNBs with Au/Pt NPs

Approximately 1000 mg of CNBs was generated from 100 ml of benzene after 30 minutes of SPP processing. The morphology of the CNBs was observed using SEM and TEM. This showed that the CNBs were spherical in shape, with a uniform size ranging from 20 nm to 30 nm; the CNBs were found to exist in a chain-like morphology (Fig. 2a and b). The principle how CNBs have agglomerated can be understood by using the diffusion limited aggregation (DLA) model like carbon black.[45] That is, when lots of CNB particles are made from plasma at the same time, these particles go through a random walk due to Brownian motion and then these particles have been interconnected in different directions by collisions of individual particles. At this time, it is suggested that the particle linkages involve the graphite layers such as heptagon/pentagon flake encapsulating particles in the necklace. Therefore, the particles are interacting with other spheres, and thus it is expected that they can be chemically linked together.[46] In the process, CNBs have been interconnected in different directions, forming a three-dimensional network. This led to the formation of both mesopores and macropores in the network. In addition, the mesopores were well connected with the macropores in all directions; these materials thus had better accessibility than microporous carbons. The HRTEM image (Fig. 2e) showed that the raw CNBs were graphitizable carbon (soft carbon); the amorphous layers in the CNBs formed long-range, highly ordered multiple graphitic layers under treatment at 1000 °C *via* the growth of aromatic networks. This morphology was unchanged after the graphitization treatments. It was concluded that the CNBs were highly stable, and did not decompose under high temperatures.

The morphology of the Au and Pt NPs was determined using bright field scanning TEM (BF-STEM) images (Fig. 2c and d, 3a and b, 4a and b). These images clearly demonstrated that the nearly spherical Au and Pt NPs were remarkably uniform, and were well dispersed over the entire surface of the CNBs. The images showed that the Au and Pt NPs had a narrow size distribution with an average size of 2–3 nm. However, larger particles of Au and Pt (*ca.* 6–7 nm) were more frequently observed after the heat treatment, which indicated that aggregation of the particles occurred at high temperatures.

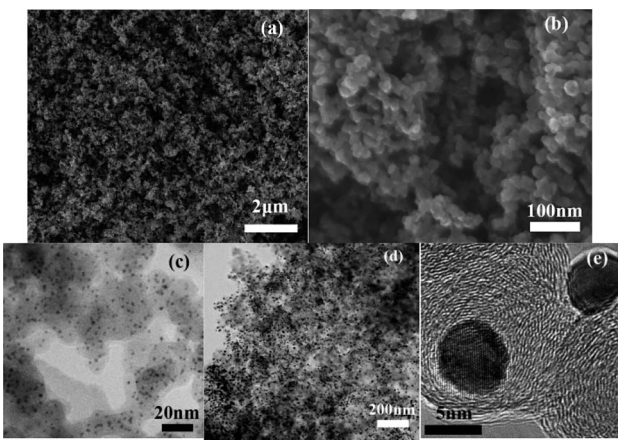

Fig. 2 (a and b) FESEM image of annealed Au/CNBs, (c) STEM image of Au/CNBs (before annealing), (d) STEM image of Au/CNBs (after annealing) and (e) HRTEM image of annealed Au/CNBs.

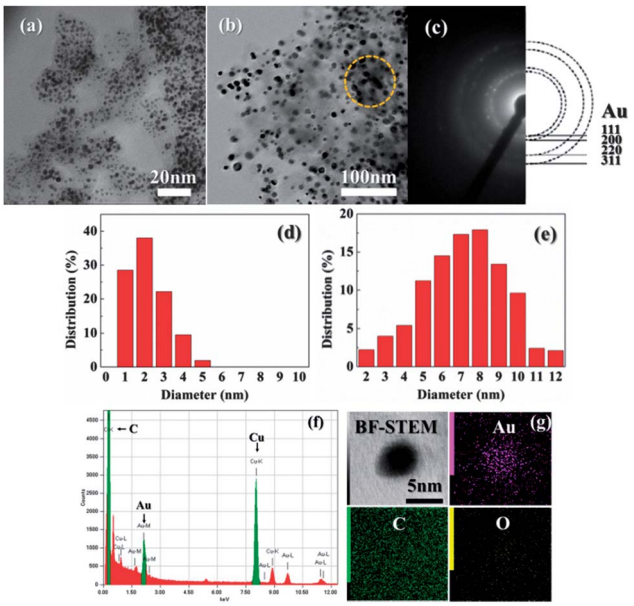

Fig. 3 TEM images of Au/CNBs fabricated using a solution plasma processing (SPP) method; (a) BF-STEM image of raw Au/CNBs; (b) BF-STEM image of annealed Au/CNBs at 850 °C under an Ar atmosphere; (c) a selected area diffraction pattern (SAED) from the yellow area in (b); (d) size distribution of raw Au NPs; (e) size distribution of annealed Au NPs; (f and g) EDS spectrum and mapping.

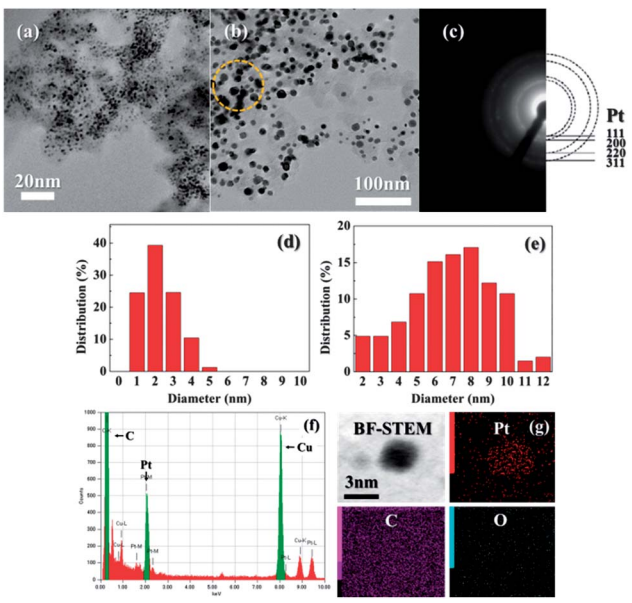

Fig. 4 TEM images of Pt/CNBs fabricated using a solution plasma processing (SPP) method; (a) BF-STEM image of raw Pt/CNBs; (b) BF-STEM image of raw annealed Pt/CNBs at 850 °C under an Ar atmosphere; (c) a selected area diffraction pattern (SAED) from the yellow area in (b); (d) size distribution of raw Pt NPs; (e) size distribution of annealed Pt NPs; (f and g) EDS spectrum and mapping.

The distribution of the NPs was confirmed using energy dispersive X-ray spectroscopy (EDS) and EDS mapping (Fig. 3f and 4f). The spectra revealed that Au and Pt were present on the CNBs, as expected; additional peaks corresponding to O and Cu were also observed. These latter peaks were artifacts that arose from the O and the Cu adsorbed on the grid on which the TEM sample was supported. EDS mapping also confirmed the presence of individual Au and Pt NPs. Fig. 3c and 4c show selected area electron diffraction patterns (SAED) obtained from the same areas displayed in Fig. 3a and 4a. This diffraction pattern was indexed as a face centered cubic (FCC) gold unit cell structure.

Characteristics of CNBs with Au/Pt NPs

The structural characterization of the Au NPs and Pt NPs was performed using XRD analysis, and typical XRD patterns are shown in Fig. 5. Five peaks were observed, corresponding to the 111, 200, 220, 311, and 222 reflections of the FCC structure of the polycrystalline Au and Pt NPs (JCPDS 04-0784, JCPDS 87-0647); these results agreed with the SAED patterns. The XRD pattern suggested that the Au and Pt NPs formed by SPP were composed of purely crystalline structures.

The average particle size of the Au and Pt NPs was calculated based on the broad peak areas from the XRD pattern using Scherrer's formula $d = 0.9\lambda/\beta\cos\theta$, where 0.9 is the shape factor generally taken for a cubic system, λ is the X-ray source wavelength, which is typically 0.154 nm, β is the full width at half maximum intensity in radians, and θ is the Bragg angle.[47] The average crystallite sizes for the Au and Pt NPs are summarized in Table 1.

Both types of NPs were smaller than 5 nm after SPP, and the size slightly increased from 5 to 9 nm after the heat treatment. These results agreed with the TEM observations. It should be noted that the broad peaks in the XRD were formed from several sharp peaks that overlapped in the same area. One of the sharp peaks was attributed to abnormally large NPs, which were observed very rarely in the TEM images. Based on the calculations from the peak area, the size of these particles was in the range of approximately 20 to 30 nm. We believe that these large particles were occasionally generated by locally concentrated sputtering on the surface electrode.

The shape of the particles was determined by comparing the 111 and 200 diffraction intensities. For the Au NPs, the intensity ratio (determined from the broad peaks) between the 200 and 111 diffractions was 0.42, which was lower than the bulk intensity ratio of 0.53 [JCPDS 04-0784].[48] This ratio remained constant after the NPs were subjected to the heat treatment. The results indicated that the synthesized Au NPs were primarily composed of 111 planes. Thus, the Au NPs produced using SPP were rich in 111 planes, and the 111 plane of the Au NPs was preferentially oriented parallel to the surface of the supporting material. According to density functional theory (DFT) results, Au 111 is the most active surface for the Li-based oxygen reduction reaction (Li-ORR).[49] It is therefore expected that the Au NPs synthesized using SPP would be highly effective catalysts in Li-ORR for Li-air battery applications.

For Pt NPs, the intensity ratio between the 200 and 111 diffractions was 0.75, which was larger than the conventional bulk intensity ratio of 0.53 [JCPDS 87-0647].[50] This indicated that the synthesized Pt NPs, which were primarily bound by 100 planes, are inclined to preferentially orient parallel to the supporting substrates. Pt 110 was found to be the most effective catalyst for the ORR in sulfuric acid electrolytes.[51] We therefore expect that the Pt NPs synthesized using SPP would enhance the efficiency of the ORR in sulfuric acid electrolytes for fuel cell applications.

Other structural specifications including the total surface area, total pore volume, and mean pore diameter of the Au/CNBs and Pt/CNBs were determined using the BET method. Fig. 6 shows the N_2 adsorption–desorption isotherms for the Au/CNBs and Pt/CNBs, respectively. According to the IUPAC classification, the N_2 adsorption isotherms for all of the samples exhibited type IV characteristics.[52] The nitrogen adsorption isotherms for the CNBs could be divided into three parts, as shown in Fig. 6, which suggested a multi-stage adsorption process. The first region (I) represented the filling of the micropores; the adsorbed amounts increased after the annealing process. The proportion of micropores was relatively low, indicating that the CNBs contained only a few micropores. In part II, the mild slope of plateau was due to multilayer adsorption on the external surface. A steep sloping curve with a narrow hysteresis loop was observed at higher relative pressures in part III, where $P/P_0 = 0.86$ to 0.98, a feature that is typically

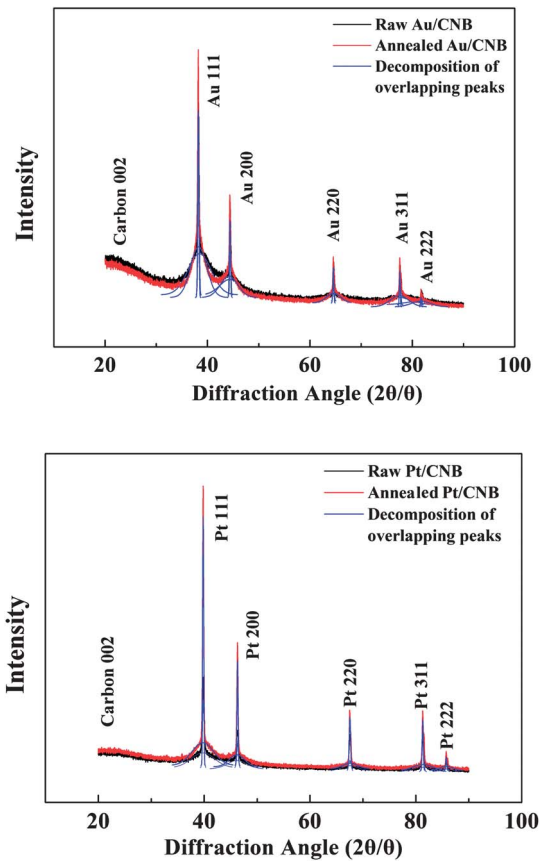

Fig. 5 X-ray diffraction patterns for NP/CNBs.

Table 1 Particle size of NPs (calculated from the broad peak)

		Crystallite size (nm)		Average crystallite size (nm)	
2Ø	Plane	Au/CNB (raw)	Au/CNB (annealed)	Au/CNB (raw)	Au/CNB (annealed)
38.2	1 1 1	2.6	5.6	3.0	5.9
44.2	2 0 0	3.0	5.3		
64.6	2 2 0	4.0	7.1		
77.4	3 1 0	2.7	5.9		
2Ø	Plane	Pt/CNB (raw)	Pt/CNB (annealed)	Pt/CNB (raw)	Pt/CNB (annealed)
39.7	1 1 1	2.0	4.3	3.2	6.7
46.1	2 0 0	2.5	6.4		
67.5	2 2 0	3.4	7.1		
81.3	3 1 0	2.9	6.2		

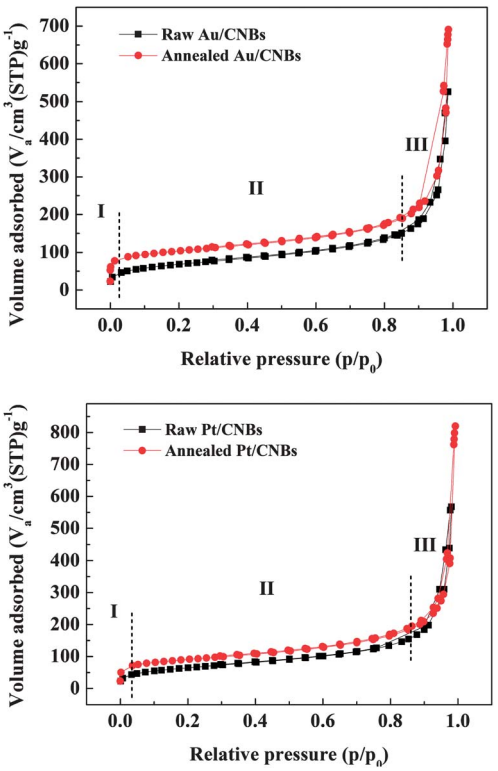

Fig. 6 Nitrogen adsorption–desorption isotherms for NP/CNBs.

associated with capillary condensation and evaporation within mesopores. These results indicated that the CNBs possessed mesopores with a very large pore volume to accommodate N_2 molecular and cylindrical slit-type pore structure characteristics.[53,54] It is assumed that these mesopores were inter-particle voids (textural mesopores) between the primary particles. In comparison, the N_2 adsorption–desorption amounts for the NP/CNBs increased significantly after the annealing treatment, for both the Au and Pt NP systems.

The structural parameters of the Au/CNBs and Pt/CNBs, including the BET surface area, total pore volume, and mean pore diameter, are shown in Table 2. The BET surface area and total pore volume for the Au/CNBs and Pt/CNBs before annealing were calculated to be 241 $m^2\ g^{-1}$ and 0.81 $cm^3\ g^{-1}$, and 233 $m^2\ g^{-1}$ and 0.87 $cm^3\ g^{-1}$, respectively. These parameters increased to 369 $m^2\ g^{-1}$ and 1.06 $cm^3\ g^{-1}$, and 320 $m^2\ g^{-1}$ and 1.17 $cm^3\ g^{-1}$, respectively, with an annealing temperature of 850 °C.

This phenomenon can be explained as follows. As shown in Fig. 6, the shape of nitrogen adsorption–desorption isotherms is not changed even after the annealing process excluding region (I). The region (I) represented the filling of the micropores and it was almost increased twice after the annealing process. To confirm the change in the elemental composition, CHN (Carbon Hydrogen Nitrogen) Corder Elemental analyzer (YANACO MT-6, Japan) was used. It determines the percent, by weight, of carbon, hydrogen, and nitrogen contained in materials. Table 3 shows the result of CHN Corder and indicates that the hydrogen containing in CNBs was almost removed and the ratio of carbon and NPs (putative) was not changed. Therefore, it is expected that a lot of micropores was created by decomposition of hydrogen gas and it caused an increase of surface area and decrease of mean pore diameter. Nevertheless, the

Table 2 Structural parameters of NP/CNBs

Sample	Surface area ($m^2\ g^{-1}$)	Pore volume ($cm^3\ g^{-1}$)	Mean pore diameter (nm)
Au/CNBs (raw)	241	0.81	15.05
Au/CNBs (annealed)	369	1.06	13.61
Pt/CNBs (raw)	233	0.87	16.70
Pt/CNBs (annealed)	320	1.17	13.52

Table 3 Weight percent of C and H elements in a compound

Sample	Carbon	Hydrogen	Nitrogen
Au/CNBs (raw)	87.41	1.80	—
Au/CNBs (annealed)	88.82	0.10	—
Pt/CNBs (raw)	87.62	1.84	—
Pt/CNBs (annealed)	88.55	0.16	—

mean pore diameter is large which ranged between 13 and 16 nm for all of the samples, because the carbon supports contained mainly mesopores. It means that chemical species could easily diffuse inside the surface of carbon materials.

Cyclic voltammetry of CNBs with Au/Pt NPs

The NP/CNBs were tested for their electrocatalytic activity in oxygen reduction reactions, which are important in the field of energy applications.[6–8,55,56] Fig. 7 shows the voltammetric responses of the Au/CNBs and Pt/CNBs with the as-prepared samples, respectively, over the potential range from −0.2 to 1.4 V.

The as-prepared samples show little electrocatalytic area than the annealed sample because their resistivity is larger than that of the annealed sample due to its low crystallinity. To confirm the electrical resistivity of NP/CNBs, the four-point probe method was applied. To prepare specimens, 60 wt% of NP/CNBs was mixed with 40 wt% of a polymer binder (PVDF, polyvinylidene fluoride, average M_w 534 000, Aldrich, Japan) by using a mortar and pestle for 10 minutes. After mixing, the powders were placed into a round die of inner diameter 10 mm, and compressed with a force of 8 MPa of pressure at 25 °C for 5 min. The composite powder was compacted to pellets of 2 mm thickness and 10 mm diameter and the measurements were conducted on these pellets. Table 4 shows the results and it indicate that the resistivity of NP/CNBs is increased after the annealing process.

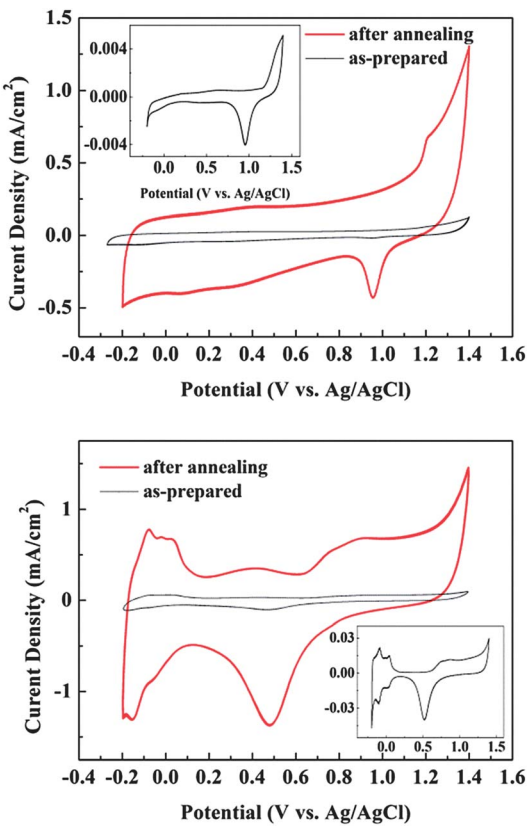

Fig. 7 Cyclic voltammetry plots for Au/CNBs (up), Pt/CNBs (down), and their corresponding bulk metal electrode (inset image).

Table 4 Electrical resistivity of NP/CNBs

Sample	Resistivity (Ω m^{-1})
Au/CNBs (raw)	956.4
Au/CNBs (annealed)	3.56
Pt/CNBs (raw)	939.1
Pt/CNBs (annealed)	4.32

Meanwhile, in the case of the Au/CNBs, Au oxide formation was observed in the range of 1.2–1.4 V regardless of the annealing process, and the reduction of Au oxide was shown between 1.0 and 0.8 V with a scan rate of 100 mV s^{-1}. These characteristics were very similar to those of a bulk gold metal electrode. The typical oxidation and reduction features in the graph indicated the successful loading of NPs on the CNB surfaces.

As shown in Fig. 7, the voltammetric features of the Pt/CNBs were also similar to the typical characteristics of bulk platinum metal electrodes. The Pt oxide formation appeared in the range of 0.65–1.4 V, while the reduction of Pt oxide occurred between 0.1 and 0.5 V. The adsorption and deposition of hydrogen occurred between 0.05 and −0.2 V with a scan rate of 100 mV s^{-1}. Furthermore, the results showed a sharp and clear cathodic current. This indicated the high electrocatalytic activity of the Pt/CNB and Au/CNB electrodes in the oxygen reduction reaction, which is an important factor for catalytic reactions.

Proposed mechanism for the one-step synthesis of NP/CNBs by SPP

The formation mechanism for the NP/CNBs was hypothesized as follows: by increasing up to the breakdown voltage, the initiation of the discharge will be started at the edge of both electrodes. From the plasma region, various radicals such as C, C_2, CH and Hα were generated.

Typical optical spectra are shown in Fig. 8. The optical emission spectra were measured from the plasma discharge zone in benzene. The major emitted wavelengths identified in this study were C_2 in the range of 468, 513 and 554 nm.[45] This C_2 radical is considered to be a very important precursor in the growth of carbon materials.[58–60] Another weaker intensity of wavelength between 431 nm was also observed. It might correspond to the excited CH radicals.[61,62] The peak of 657 nm was possibly generated by active species of Hα. These radical generation processes can be considered as follows. When the benzene was gasified and excited, the resonance of the double bond of the benzene ring was broken at first and became an open ring structure. The open chain structure was further excited and finally the active species such as H, C_2 and CH can be generated in the plasma. It is assumed that these radicals were created in multiple steps of dissociation and recombination.[63] The optical emission spectrum as well as the identification of active species similar to the current experimental setup has been published.[64]

It should be noted that gold and platinum particles generated from the sputtering of the electrodes were not observed in

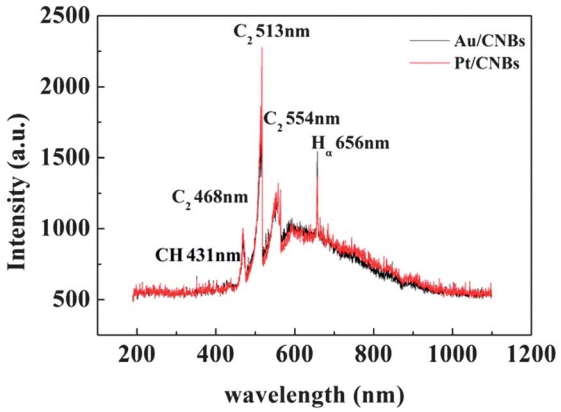

Fig. 8 Optical emission spectrum obtained from liquid discharge zone in benzene.

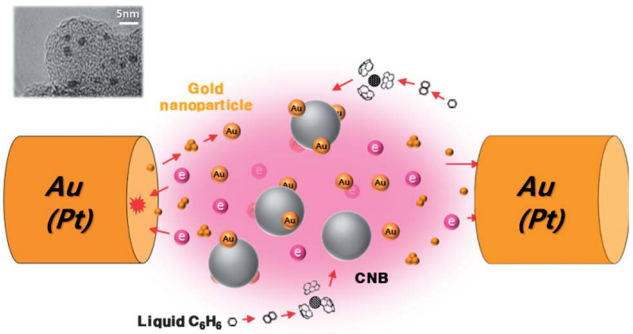

Scheme 1 Formation mechanism of NP/CNBs.

the spectrum. However, the existence of the metal NPs was clearly supported by the results of TEM and Inductively Coupled Plasma-Atomic Emission Spectrometry (ICP AES, see ESI Fig. S3†).

In order to understand the chemical reaction carried out by radicals in benzene solution, a detailed liquid analysis has been carried out by GC–MS with the plasma process time intervals of 2 seconds, 40 seconds, 60 seconds and 3 min. All of the intermediates were identified and their chemical formulae were illustrated and listed in the ESI (see ESI Fig. S5 and Table S3†). It showed that the intermediates were synthesized at the beginning of the process (time = 2 s). With an increasing process time, these intermediates reacted further with the radicals, and the by-products became more complicated.

Meanwhile, the way in which nucleation of carbon atoms/radicals gives large spheres is unclear. One of the most widely discussed proposals is the nucleation from a pentagonal carbon ring followed by a spiral shell growth.[65–68] (see ESI Fig. S6 and S7†). It can be considered to be a development of four processes: (a) nucleation of a pentagon, (b) growth of a quasi-icosahedral shell, (c) formation of a spiral shell carbon particle and (d) growth of a large size carbon sphere. With the information obtained from OES and GC-MS, the process of nucleation of carbon, the growth of SPP synthesized CNBs can also be considered in the same manner. In GC-MS, we can identify decisive evidence for compounds which can be used as precursors of growth of a quasi-icosahedral shell such as 5*H*-benzocycloheptene, 6,7-dihydro-, acenaphthene, anthracene, acenaphthylene, azulene, benzo[*ghi*]fluoranthene, cyclopenta(*cd*)pyrene, 3,4-dihydro-, cyclopenta[*cd*]pyrene, cyclopentane, ethyl-, fluorene, fluoranthene and indene. It is expected that carbon spheres can be easily synthesized by a solution plasma process because pentagonal carbon-rings are essential for forming carbon sphere structures.

Meanwhile, numerous novel metal atoms (*i.e.*, Au and Pt) were also generated from the electrode surfaces under sputtering, because the electrodes were continuously bombarded by energetic electrons. These atoms formed small metal particles that were loaded onto the carbon spheres, as shown in Scheme 1. The synthesized NP/CNBs aggregated through diffusion-limited aggregation.[57] The void volumes between the particles in the aggregates (intra-aggregate voids) and between the aggregates were filled with liquid benzene as soon as this cluster exited the plasma zone. As a result, mesopores were formed in the networks of NP/CNBs.

Conclusions

Noble nanoparticles (NPs) supported on spherical carbon nanoparticles were successfully fabricated from metal electrodes *via* a one-step solution plasma process in benzene at atmospheric pressure. In order to increase the conductivity of the material, an annealing process has been conducted. The morphology of the CNBs was spherical, with uniform sizes ranging from 20 nm to 30 nm, and the CNBs were found to form a chain-like morphology. The structural characteristics proved that the synthesized CNBs had an excellent pore structure, with an average diameter ranging between 13 and 16 nm and a total pore volume ranging between 1.06 and 1.17 $cm^3\ g^{-1}$. TEM images showed that spherical Au and Pt NPs were uniformly and highly dispersed over the entire surface of the CNBs, and the average particle size was below 10 nm after heat treatment. Cyclic voltammetry showed clear peaks corresponding to the oxidation and reduction features in the catalytic reaction. This indicated the high electrocatalytic activity of the Pt/CNB and Au/CNB electrodes in the oxygen reduction reaction, which is an important factor in terms of catalytic reactions. This method proved that SPP is a simple method for the large-scale synthesis of NP/carbon. Therefore, SPP holds great potential as a candidate for next-generation synthetic methods for the production of NP/carbon materials. An additional benefit of this method is that it can be used to synthesize all types of NPs (including bimetallic NPs) on the supporting carbon, simply by changing the metal in the electrodes.

Notes and references

1 G. G. Wildgoose, C. E. Banks and R. G. Compton, *Small*, 2006, **2**, 182.
2 V. Georgakilas, D. Gournis, V. Tzitzios, L. Pasquato, D. M. Guldi and M. Prato, *J. Mater. Chem.*, 2007, **17**, 2679.
3 X. G. Hu and S. J. Dong, *J. Mater. Chem.*, 2008, **18**, 1279.

4 D. Vairavapandian, P. Vichchulada and M. D. Lay, *Anal. Chim. Acta*, 2008, **626**, 119.
5 X. Peng, J. Chen, J. A. Misewich and S. S. Wong, *Chem. Soc. Rev.*, 2009, **38**, 1076.
6 Y. C. Lu, Z. Xu, H. A. Gasteiger, S. Chen, K. Hamad-Schifferli and Y. Shao-Horn, *J. Am. Chem. Soc.*, 2010, **132**, 12170.
7 Y. C. Lu, H. A. Gasteiger, E. Crumlin, R. McGuire and Y. Shao-Horn, *J. Electrochem. Soc.*, 2010, **157**, A1016.
8 Y. C. Lu, H. A. Gasteiger, M. C. Parent, V. Chiloyan and Y. Shao-Horna, *Electrochem. Solid State Lett.*, 2010, **13**, A69.
9 B. H. Wu, D. Hu, Y. J. Kuang, B. Liu, X. H. Zhang and J. H. Chen, *Angew. Chem., Int. Ed.*, 2009, **48**, 4751.
10 W. Z. Li, X. Wang, Z. W. Chen, M. Waje and Y. S. Yan, *J. Phys. Chem. B*, 2006, **110**, 15353.
11 S. Y. Wang, S. P. Jiang, T. J. White, J. Guo and X. Wang, *J. Phys. Chem. C*, 2009, **113**, 18935.
12 A. Y. Stakheev and L. M. Kustov, *Appl. Catal. A*, 1999, **188**, 335.
13 K. Kinoshita, *J. Electrochem. Soc.*, 1990, **137**, 845.
14 F. Maillard, M. Eikerling, O. V. Cherstiouk, S. Schreier, E. Savinova and U. Stimming, *Faraday Discuss.*, 2004, **125**, 357.
15 F. Maillard, S. Schreier, M. Hanzlik, E. R. Savinova, S. Weinkauf and U. Stimming, *Phys. Chem. Chem. Phys.*, 2005, **7**, 385.
16 Y. Xie, R. Ye and H. Liu, *Colloids Surf., A*, 2006, **279**, 175.
17 M. Maillard, S. Giorgo and M. P. Pileni, *Adv. Mater.*, 2002, **14**, 1084.
18 Z. S. Pillai and P. V. Kamat, *J. Phys. Chem. B*, 2004, **108**, 945.
19 K. Patel, S. Kapoor, D. P. Dave and T. J. Murherjee, *J. Chem. Sci.*, 2005, **117**, 53.
20 R. A. Salkar, P. Jeevanandam, S. T. Aruna, Y. Koltypin and A. Gedanken, *J. Mater. Chem.*, 1999, **9**, 1333.
21 B. Soroushian, I. Lampre, J. Belloni and M. Mostafavi, *Radiat. Phys. Chem.*, 2005, **72**, 111.
22 M. Starowicz, B. Stypula and J. Banaœ, *Electrochem. Commun.*, 2006, **8**, 227.
23 J. J. Zhu, X. H. Liao, X. N. Zhao and H. Y. Hen, *Mater. Lett.*, 2001, **49**, 91.
24 S. Liu, S. Chen, S. Avivi and A. Gendanken, *J. Non-Cryst. Solids*, 2001, **283**, 231.
25 Y. Zhang, A. M. Valiente, I. R. Ramos, Q. Xin and A. G. Ruiz, *Catal. Today*, 2004, **93–95**, 619.
26 C. W. Hills, N. H. Mack and R. G. Nuzzo, *J. Phys. Chem. B*, 2003, **107**, 2626.
27 J. T. Moore, J. D. Corn, D. Chu, R. Jiang, D. L. Boxall, E. A. Kenik and C. M. Lukehart, *Chem. Mater.*, 2003, **15**, 3320.
28 G. C. Bond and D. T. Thompson, *Catal. Rev. Sci. Eng.*, 1999, **41**, 319.
29 R. Zanella, S. Giorgio, C. H. Shin, C. R. Henry and C. J. Louis, *J. Catal.*, 2004, **222**, 357.
30 F. Moreau, G. C. Bond and A. O. Taylor, *J. Catal.*, 2005, **231**, 105.
31 U. A. Paulus, U. Endruschat, G. J. Feldmeyer, T. J. Schmidt, H. Bönnemann and R. J. Behm, *J. Catal.*, 2000, **195**, 383.
32 H. Bönnemann, R. Brinkmann, S. Kinge, T. O. Ely and M. Armand, *Fuel Cells*, 2004, **4**, 289.
33 M. T. Reetz and M. G. Koch, *J. Am. Chem. Soc.*, 1999, **121**, 7933.
34 X. Wang and I. Hsing, *Electrochim. Acta*, 2002, **47**, 2981.
35 T. Kim, M. Takahashi, M. Nagai and K. Kobayashi, *Electrochim. Acta*, 2004, **50**, 817.
36 J. Solla-Gullon, F. J. Vidal-Iglesias, V. Montiel and A. Aldaz, *Electrochim. Acta*, 2004, **49**, 5079.
37 L. Xiong and A. Manthiram, *Solid State Ionics*, 2005, **176**, 385.
38 S. Rojas, F. J. Garcia, S. Jaras, M. V. Huerta, J. L. F. Fierro and M. Boutonnet, *Appl. Catal., A*, 2005, **285**, 24.
39 S. Nomura, H. Toyata, S. Mukasa, H. Yamashita, T. Maehara and M. Kuramoto, *Appl. Phys. Lett.*, 2006, **88**, 1502.
40 K. Imasaka, Y. Kanatake, Y. Ohshiro, J. Suehiro and M. Hara, *Thin Solid Films*, 2006, **506–507**, 250.
41 G. Saito, S. Hosokai, M. Tsubota and T. Akiyama, *J. Appl. Phys.*, 2011, **110**, 3302.
42 J. Hieda, N. Saito and O. Takai, *J. Vac. Sci. Technol., A*, 2008, **26**, 854.
43 S. P. Cho, M. A. Bratescu, N. Saito and O. Takai, *Nanotechnology*, 2011, **22**, 5701.
44 M. A. Bratescu, S. P. Cho, O. Takai and N. Saito, *J. Phys. Chem. C*, 2011, **115**, 24569.
45 T. A. Witten and L. M. Sander, *Phys. Rev. Lett.*, 1981, **47**, 1400.
46 D. B. Buchholz, S. P. Doherty and R. P. H. Chang, *Carbon*, 2003, **41**, 1625.
47 L. V. Azaroff, *Elements of X-Ray Crystallography*, McGraw-Hill, NewYork, USA, 1968, p. 549.
48 F. Kim, S. Connor, H. Song, T. Kuykendall and P. Yang, *Angew. Chem., Int. Ed.*, 2004, **43**, 3673.
49 Y. Xu and W. A. Shelton, *J. Chem. Phys.*, 2010, **133**, 024703.
50 E. Teliz, V. Díaz, R. Faccio, A. W. Mombru and C. F. Zinola, *Int. J. Electrochem.*, 2011, **2011**, 289032.
51 A. Atkinson, R. I. Taylor and A. E. Hughes, *Philos. Mag. A*, 1982, **45**, 823.
52 J. Rouquerol, D. Avnir, C. W. Fairbridge, D. H. Everett, J. M. Haynes, N. Pernicone, J. D. F. Ramsay, K. S. W. Sing and K. K. Unger, *Pure Appl. Chem.*, 1994, **66**, 1739.
53 H. M. Kao, T. Y. Shen, J. D. Wu and L. P. Lee, *Microporous Mesoporous Mater.*, 2008, **110**, 461.
54 Y. Wang, S. Zhu, Y. Mai, Y. Zhou, X. Zhu and D. Yan, *Microporous Mesoporous Mater.*, 2008, **114**, 222.
55 J. O. M. Bockris and S. Srinivasan, *Fuel Cell, Their Electrochemistry*, McGraw-Hill, New York, USA, 1969.
56 K. Kinoshita, *Carbon, Electrochemical and Physico Chemical Properties*, Wiley, New York, USA, 1988.
57 A. M. Zhu, X. L. Zhang, X. S. Li and W. M. Gong, *Sci. China, Ser. B: Chem.*, 2002, **45**, 426.
58 P. Gopinath and J. Gore, *Combust. Flame*, 2007, **151**, 542.
59 J. Khachan, B. W. James and A. Marfoure, *Appl. Phys. Lett.*, 2000, **77**, 2973.
60 A. N. Goyette, J. E. Lawler, L. W. Anderson, D. M. Gruen, T. G. McCauley and D. Zhou, *Plasma Sources Sci. Technol.*, 1998, **7**, 149.
61 A. M. Huang, G. G. Xia, J. Y. Wang and S. L. Suib, *J. Catal.*, 2000, **189**, 349.

62 C. J. Liu, B. Z. Xue and B. Eliasson, *Plasma Chem. Plasma Process.*, 2001, **21**, 301.
63 T. Yamamoto, *Moon Planets*, 1981, **24**, 453–463.
64 O. L. Li, J. Kang, K. Urashima and N. Saito, *Int. J. Environ. Sci. Technol.*, 2013, **7**, 31.
65 Z. C. Kang and Z. L. Wang, *Philos. Mag. B*, 1996, **73**, 905.
66 Z. C. Kang and Z. L. Wang, *J. Phys. Chem. B*, 1996, **100**, 5163.
67 Z. L. Wang and Z. C. Kang, *J. Phys. Chem.*, 1996, **100**, 17725.
68 H. W. Kroto and K. McKay, *Nature*, 1988, **331**, 328.